

Bullet Cluster: Remarkable Revelations and Enduring Insights – Part I

Siddharth Savyasachi Malu^{1,3*} and Sanjay K. Pandey^{2,4}

¹*Dept. of Astronomy, Astrophysics and Space Engineering, IIT Indore, Simrol, Khandwa Road, Indore 453552 India*

²*Sri Lal Bahadur Shastri Degree College, Gonda India*

8 March 2024

ABSTRACT

This study unveils new insights into the Bullet Cluster through cm-wave observations made with the Australia Telescope Compact Array, focusing on the Sunyaev-Zel’dovich Effect (SZE). A novel SZE feature was discovered, distinctively offset from the X-ray brightness peak, challenging conventional associations between such phenomena. The findings, achieved through high-resolution interferometric imaging, reveal complex substructures within the SZE, including significantly displaced components uncorrelated with X-ray, optical, or lensing maps. This deviation underscores the complexity within the cluster’s dynamics and suggests that detailed, high-resolution SZE imaging is crucial for understanding the physics of merging clusters. We perform several tests to ensure that one of these novel and unusual features is indeed real, and that the detection of all features in the images is robust. In addition to these displacements, we find several SZE features that are tentatively located at critical boundaries in this merging cluster - these features will be discussed in the next few manuscripts in this series. These observations pave the way for more sophisticated analyses, combining SZE and X-ray data, to decode the evolutionary mysteries of cosmic structures like the Bullet Cluster. We note here that we are discussing only one novel / peculiar feature in the observations of the cluster done in the year 2019. Further observations have revealed more features, which we shall discuss in the next few manuscripts in this series on the Bullet cluster.

Key words: cosmic background radiation — galaxies: clusters: individual (1E 0657–56, RX J0658–5557) — intergalactic medium — radio continuum: general — techniques: interferometric

1 INTRODUCTION

The Sunyaev–Zeldovich effect (SZE) is the inverse Compton scattering of CMB photons off a collection of electrons which causes a spectral distortion in the CMB (Sunyaev & Zeldovich 1972). This inverse Compton scattering causes a decrease in CMB brightness at frequencies below 217 GHz and an increase above 217 GHz. The amplitude of the decrease in brightness is given by $\Delta T \propto \int n_e T_e dl^1$, where the integral is along the line of sight. Galaxy clusters are the largest gravitationally bound objects and the largest sources of hot, dense ionized gas, which makes them ideal targets for studying through the SZE, especially since the SZE is independent of redshift.

1E0657–56, known as the **Bullet Cluster**, is one of the hottest known clusters that has been well-studied over the

last decade for a variety of reasons; namely, the existence of a strong radio halo (Liang et al. 2000), the Sunyaev-Zel’dovich effect (Halverson et al. (2009), Plagge et al. (2010) and references therein), its X-ray brightness (Markevitch et al. 2002), though most notably in providing the most direct proof of the existence of dark matter (Clowe et al. 2006). It is a cluster collision/merger event at $z \sim 0.296$, with the larger, westward cluster being ~ 10 times the mass of the smaller ‘bullet’.

Cluster mergers have by now been observed in many different regimes: from X-ray observations using the *Chandra* to radio observations. Diffuse non-thermal radio emission in clusters of galaxies of $\sim \text{Mpc}$ size not associated with galaxies, when close to the centres of clusters, are called *radio halos*, and when at or close to the peripheries of clusters are called *radio relics*. These are associated with relativistic electrons and magnetic fields in the ICM and have steep synchrotron spectra ($S \propto \nu^{-\alpha}$, $\alpha > 1.0$); radio relics have steeper spectra compared to radio halos. About 35% of clusters with

* E-mail: siddharth@iiti.ac.in

¹ T_e = Electron temperature; n_e = electron number density

X-ray luminosities greater than $5 \times 10^{44} \text{ erg s}^{-1}$ have radio halos (Venturi et al 2008). However, among clusters that are dynamically disturbed, about 75% exhibit radio halos (Cassano et al 2010). The total power radiated from radio halos (at 1.4 GHz) is found to scale with X-ray luminosity and temperature. In the currently favoured model of radio halo formation, the ‘turbulent re-acceleration through merger’ model, the spectra of radio halos is expected and indeed, observed to steepen considerably at frequencies below 10 GHz. Measurements by Liang et al (2000) suggest such a steepening at ~ 8.5 GHz. The radio halo in the Bullet cluster was thus not expected to be observable at 18 GHz.

Since not many clusters at redshifts greater than 0.3 were known prior to the PLANCK satellite and MACSurvey, it has been difficult to probe the existence of a redshift evolution in the occurrence of radio halos, until now.

Two competing models exist as explanations of the origins or radio halos: the so-called *Primary* or *Turbulent Reacceleration* (see, e.g. Brunetti & Lazarian (2011); Cassano (2010); Cassano et al. (2010)) and *Secondary* models (e.g. Keshet et al. 2010). Primary models of radio halo formation feature an exponential steepening of the spectrum, or a “knee” – the exact frequency at which the “knee” occurs depends on the epoch of the cluster merger, and the age of the radio halo. This “knee” is seen at a wide range of frequencies, from 1.4 GHz to 5 GHz. In secondary models, the steepening of the spectrum is followed by a flattening, usually at frequencies higher than 9 GHz. Deep high-frequency observations (above 9 GHz) of radio halos are therefore crucial for understanding the origins of radio halos.

In this paper, we present the first 18 GHz interferometer observations of the Bullet cluster from the Australia Telescope Compact Array (ATCA) using the recently installed Compact Array Broadband Backend or CABB (Wilson et al. including S.S. Malu 2011). We present our observations in §2, describe the imaging of the cluster at 18 GHz in §3, enumerate the consistency checks run by us in §4, place limits on the SZE in §5 and discuss the SZE features in §6. It may be noted here that the interferometer imaging lacks the low spatial frequencies that are required to image the SZE effect in its entirety, and misses the extended SZE emission; therefore our image may not be useful for fitting gas models along with X-ray data. The imaging reveals, for the first time, the existence of a SZE component in the Bullet Cluster displaced from the X-ray peak, pointing to the importance and need for high angular resolution imaging of SZE in such complex merging clusters in order to usefully model the cluster gas.

Observations from the South Pole Telescope (Lueker et al. 2010) show that on arcminute and smaller scales observed CMB anisotropy power is significantly less than levels expected from models of SZE from a cosmological distribution of clusters. This discrepancy may be an indication of our lack of understanding of the environmental impact of cluster mergers. This paper presents sub-arcmin angular resolution observations of the SZE in the cluster, which demonstrates that the relation between SZE and X-ray emission is complex and requires additional physics that may be related to the impact of the merger on intracluster gas.

Table 1. Journal of the ATCA observations.

Array configuration	Observing time (hours)	Date
H168	12	2009 April 25
H168	12	2009 April 26
H168	12	2010 July 29
H168	12	2010 July 30
H75	8	2009 June 28
H75	8	2009 June 29
H75	8	2009 June 30
H75	6	2010 September 21
H75	6	2010 September 22

2 RADIO OBSERVATIONS AND IMAGING

The Australia Telescope Compact Array (ATCA) is a radio interferometer with six 22-m antennas, five of which may be positioned on stations along a ‘T’-shaped rail track that is 3-km along E-W and 214-m along N-S.

Observations were made in a pair of 2-GHz bands: a ‘17-GHz band’ covering frequencies 16-18 GHz and a ‘19-GHz band’ covering the range 18-20 GHz. Each of the 2-GHz wide bands were subdivided into 2048 frequency channels. All observations were in full polarization mode and recorded multi-channel continuum visibilities.

X-ray images of the cluster show two peaks separated by $\sim 1'.5$ and the detected extent of X-ray emission is $\sim 6'$ (Andreani et al. 1999) suggesting that hot gas pervades a significant area between and beyond the constituent clusters. Since the FWHM field-of-view of the ATCA antennas is $2'.6$ at 18 GHz, we mosaic imaged the Bullet cluster in 2009 using 2 pointing centres at (J2000 epoch coordinates) RA: $06^{\text{h}}58^{\text{m}}20^{\text{s}}$, DEC: $-55^{\circ}56'28''$ and RA: $06^{\text{h}}58^{\text{m}}30^{\text{s}}$, DEC: $-55^{\circ}56'28''$ and in 2010 using 4 pointing centres at RA: $06^{\text{h}}58^{\text{m}}32.19^{\text{s}}$, DEC: $-55^{\circ}57'00''$; RA: $06^{\text{h}}58^{\text{m}}30^{\text{s}}$, DEC: $-55^{\circ}56'00''$; RA: $06^{\text{h}}58^{\text{m}}25^{\text{s}}$, DEC: $-55^{\circ}57'00''$ and RA: $06^{\text{h}}58^{\text{m}}22.81^{\text{s}}$, DEC: $-55^{\circ}56'00''$.

Observations were made in each of two ATCA array configurations: H168 and H75 that have baselines up to 168 and 75 m respectively; the former to enable subtraction of unresolved continuum sources, the latter to provide enhanced surface brightness sensitivity for imaging of the SZE. A journal of the observations is in Table 1. In each of the observing sessions, antenna pointing corrections were updated every hour using a 5-point offset pattern observation on PKS B0537–441, the unresolved calibrator PKS B0742–56 was observed every 10 min to monitor and correct for amplitude and phase drifts in the interferometer arms, and PKS B1934–638 was observed once every session as a primary calibrator to set the absolute flux density scale. During the 10 mins between successive calibrations, the two pointing positions were sequentially observed for 90 sec each. Visibilities were recorded with 10 sec averaging.

Interferometer visibilities were examined, calibrated and imaged using MIRIAD; all image processing were also accomplished using utilities in this software package. The visibility data in the 17 and 19 GHz bands were separately edited for interference and calibrated before bandwidth synthesis imaging. Visibility data in each of the 2 GHz wide bands were recorded over 2048 frequency channels, and 50 chan-

nels at each of the band edges were excluded from analysis to avoid data in frequency domains where signal path gains are relatively low. Frequency channels that appeared to have relatively large fluctuations in visibility amplitude owing to hardware faults in the digital correlator were also rejected prior to calibration and imaging.

2.1 Calibration

Adopted fluxes for the primary calibrator PKS B1934–638 were 1.146 and 0.992 Jy in the 17 and 19 GHz bands respectively; the spectral index α (defined as $S_\nu \propto \nu^\alpha$, where S_ν is the flux density at frequency ν) was adopted to be -1.33 in both bands (see Sault (2003)). Outliers in the amplitudes of visibility data on PKS B1934–638 were rejected—removing 15% of data—and the reliable visibilities were used to set the absolute flux density scale as well as determine the instrument bandpass calibration. When calibrated for the bandpass, the visibility amplitudes of PKS B0742–56 showed continuity across the 4-GHz observing frequency range and a trend consistent with a single power-law: this was a check of the bandpass calibration. Drifts of up to 30° were observed in the interferometer arms over the observing sessions: calibrations for the time-varying complex gains in the antenna signal paths as well as calibrations for polarization leakages were derived from the visibilities on PKS B0742–56. RMS phase variations in antenna signal paths within the 1-min calibrator scans was within 10° , indicating that short timescale atmospheric and instrumental phase cycling would not result in amplitude attenuation of more than 3%.

Since no circular polarization is expected, Stokes V is expected to be consistent with thermal noise. Therefore, at times and frequency channels where Stokes V visibilities deviate more than four times rms thermal noise in the calibrated visibilities acquired towards the Bullet cluster pointings, data in all Stokes parameters were rejected. Stokes-V based clipping was therefore done, aimed at automated rejection of self-generated low level interference.

2.2 Imaging

Multi-channel continuum visibilities in both bands and both pointings were imaged together to form a wide-field multi-frequency synthesis mosaic image of the Bullet cluster shown in Fig. 1. The image displayed has been truncated where the attenuation in the mosaic image owing to the primary beam—and consequently the response to source flux density—falls below 10%. The mosaic image was made with a beam of FWHM $20'.8 \times 14'.5$ at 89° position angle (P.A.), and has an rms noise that is $5.5 \mu\text{Jy beam}^{-1}$ at the centre and increases by factor five to the edges of the field of view. The rms noise in the image was estimated from Stokes V data and is consistent with expectations based on the system temperature during the observations, bandwidth and integration time. The image displayed has been tapered to make the rms noise uniform over the field of view.

Discrete sources detected by Liang et al. (2000) at 1.344 GHz are marked using symbols ‘A’ through ‘H’. All these eight sources are detected in the 18 GHz mosaic image at a level exceeding two standard deviation in image thermal noise. The brightest source in our 18-GHz image is at

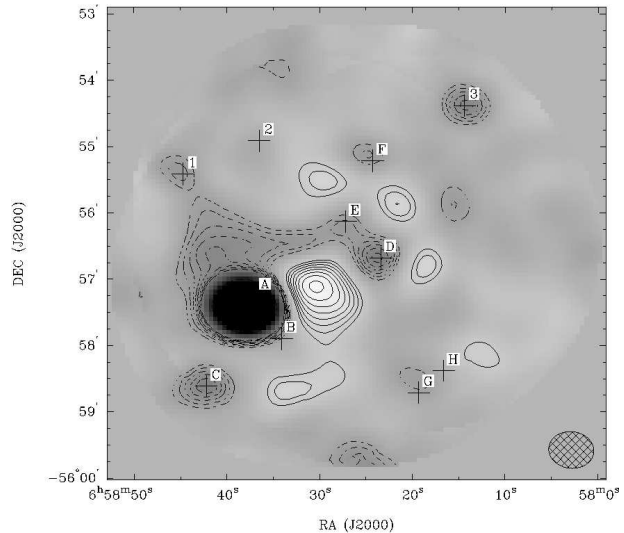


Figure 1. 18 GHz mosaic image of the Bullet cluster. In this representation as well as subsequent images displayed herein the image has been tapered to make the rms noise uniform over the field of view; this results in an attenuation of unresolved sources by factor 0.02 at the edge. Image rms noise is $6.5 \mu\text{Jy beam}^{-1}$; the beam FWHM is $39'.8 \times 32'.1$ at 87.3° P.A. and is shown using a filled ellipse in the lower right corner. Contour levels are at $\pm(3,4,5,6,7,8,9,10)$ times the rms noise. Locations of discrete sources detected by Liang et al. (2000) and in this image are marked with cross symbols. This image, and the two images that follow have been deconvolved. Errors due to sidelobes are not significant, as calculated and discussed in the text. In this image, and all subsequent images, light regions and solid contours indicate $-ve$ features; dark regions and dashed contours $+ve$ features.

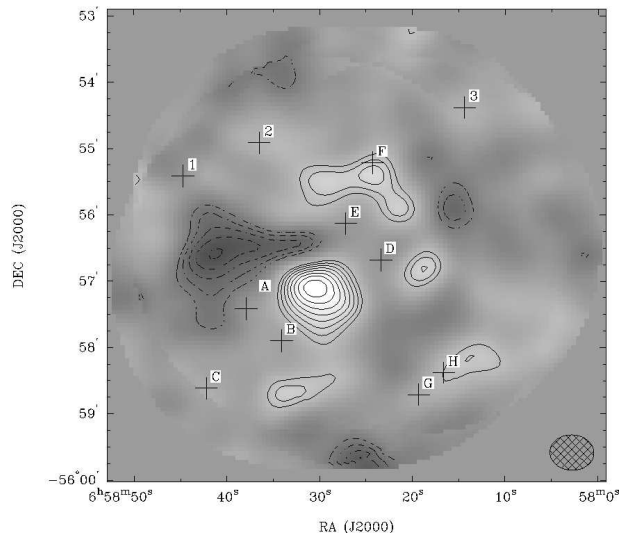


Figure 2. 18 GHz mosaic image of the bullet cluster with unresolved continuum sources subtracted. The beam FWHM and rms noise are same as for figure 1. Contour levels are at $\pm(3,4,5,6,7,8,9,10)$ times the rms noise. Locations of discrete sources detected by Liang et al. (2000) and in our 18 GHz data are marked with cross symbols.

RA: $06^{\text{h}}58^{\text{m}}37^{\text{s}}.9$, DEC: $-55^{\circ}57'25''$ and is marked ‘A’ in the figure; this is a LIRG high- z galaxy (Rex et al. 2009) and is detected with a flux density of 1.69 ± 0.04 mJy at 18 GHz.

3 IMAGING THE BULLET CLUSTER AT 18 GHZ

Radio images of the cluster field include discrete radio sources, a radio halo (Liang et al. 2000), and SZE (Halverson et al. 2009; Plagge et al. 2010) that is expected to appear as a decrement at the ATCA observing frequencies. For the characterization of the SZE decrement and the Radio Halo, it is essential to accurately subtract all discrete sources.

3.1 Subtraction of unresolved continuum sources

The image in Fig. 1 was made with visibility weighting close to natural in order to have low rms noise and good surface brightness sensitivity. To characterize first the unresolved continuum sources in the field, we constructed a separate image with uniform weighting of the visibilities that has a factor of two greater rms noise but, importantly, de-emphasizes extended halo emission and SZE. Sky regions that have image intensity exceeding four times the rms noise in Fig. 1 were examined for unresolved sources. Apart from sources ‘A’ through ‘H’, three sources were detected with flux density exceeding four times the rms noise in the uniformly weighted image; these are marked ‘1’ through ‘3’ in Fig. 1. Of these, sources ‘1’ and ‘2’ are undetected in the 1.344 GHz image and are likely to have relatively flatter spectra. The flux densities of the 11 unresolved continuum sources in the field were estimated from the image made with uniform weighting and subtracted from the visibility data.

A mosaic image of the cluster made with natural weighting and using visibilities from which unresolved continuum sources were subtracted is in Fig. 2. The beam FWHM and rms noise distribution and taper are same as for Fig. 1.

Positions of all the sources subtracted have been marked in Fig. 1 and in Table 3 we list the positions and 18-GHz flux densities. A negative feature appears close to the location where source ‘F’ was subtracted; this is an extended negative feature that is absent in the higher resolution images made with uniform visibility weighting. The brightest positive feature in this residual image is extended emission with a peak of $40 \mu\text{Jy beam}^{-1}$ at RA: $06^{\text{h}}58^{\text{m}}31^{\text{s}}.1$, DEC: $-55^{\circ}56'27''$; this is 18-GHz emission from the radio halo, which was previously discovered by Liang et al. (2000). At RA: $06^{\text{h}}58^{\text{m}}31^{\text{s}}.7$, DEC: $-55^{\circ}57'04''$ is the peak negative feature; this is the centre of the SZ feature, discussed below.

3.2 The 18 GHz Bullet cluster image: Radio Halo and the SZ Effect

The 18-GHz image in Fig. 3, which has been made with a taper that represents a $39'.8 \times 32'.1$ FWHM beam, clearly shows negative intensity values towards the central regions

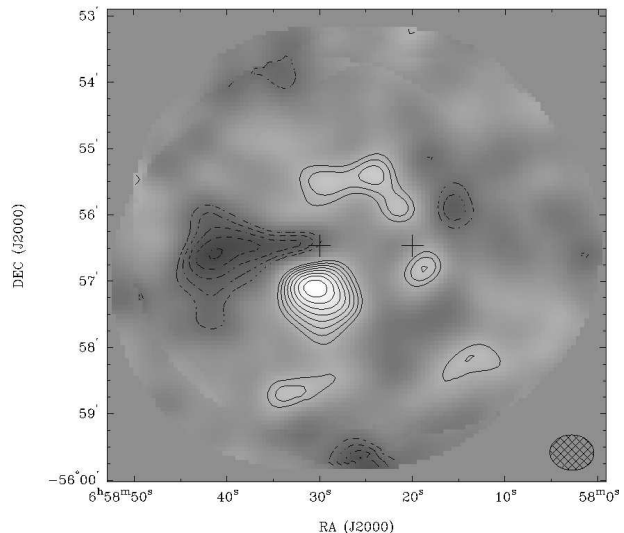


Figure 3. Source-subtracted deconvolved 18 GHz mosaic image of the bullet cluster (identical to the previous image), made with natural weighting and a uv taper corresponding to a $39'.8 \times 32'.1$ FWHM beam. Image rms noise level is $6.5 \mu\text{Jy beam}^{-1}$. Contour levels are at $\pm(3,4,5,6,7,8,9,10)$ times the rms noise. The radio halo previously detected by Liang et al. (2000) is the brightest positive feature close to the centre of the image and has a peak of 7.8σ ; the SZ effect is detected and has a peak decrement of -10.7σ to the S of the halo. Two other SZ effect features are detected to the NW regions of the halo, with a peak decrement of -5.7σ . Contrast has been adjusted in this image in order to make all contours visible. The two peaks seen in X-rays are marked. Notice the $\sim 40''$ displacement of the peak SZE decrement from the X-ray brightness peak

of the cluster. These SZE features appear to be confined within, and are bounded by the lowest intensity contours of the Radio Halo component, as can be seen in the 18-GHz image (Fig. 3) prior to any subtraction of the halo component, which would only enhance these SZE features. In this image, which has the unresolved continuum sources subtracted, there is a peak in flux density at the peak of the Radio Halo and positive 18-GHz emission towards the eastern parts of the Radio Halo. Most noteworthy is the negative peak, which may be a deep SZE feature, to the south of the peak in the expected halo contribution, at RA: $06^{\text{h}}58^{\text{m}}30^{\text{s}}.285$, DEC: $-55^{\circ}57'08''$. It may be noted that this interferometer image lacks the low spatial frequencies to reproduce the extended SZE emission, which may be missing.

The 18 GHz image made from ATCA (Fig. 3) exhibits not just the SZE (peak decrement $-84.7 \mu\text{Jy beam}^{-1}$ at -10.7σ), but also, surprisingly, the radio halo (peak 7.8σ). Radio halos are known to have spectra that steepen at frequencies less than 5 GHz. The spectral index of the radio halo in the Bullet cluster does not show any sign of steepening at frequencies lower than 8 GHz (Liang et al. 2000), and the apparent steepening at 8.8 GHz may well be due to the SZE. To the best of our knowledge, this is the first positive detection of a radio halo at any frequency above 10 GHz; further discussion of the radio halo at 18 GHz and its implications is left to a companion manuscript. Therefore, in conclusion, the SZE shown in Fig. 3 is the *least* that can be expected at 18 GHz, with a peak SZE dip of -10.7σ .

Table 2. A comparison of the SZ feature properties before and after deconvolution.

Label	RMS _{NOISE}	Intensity	Significance	Size	RA (J2000) DEC					
	($\mu\text{Jy beam}^{-1}$)	($\mu\text{Jy beam}^{-1}$)	(σ)	(3σ contour)	h	m	s	°	'	''
Before	7.0	-93.4	10.5	$56'' \times 81''$	06	58	30.762	-55	57	08
After	6.5	-84.7	10.7	$66'' \times 76''$	06	58	30.285	-55	57	08

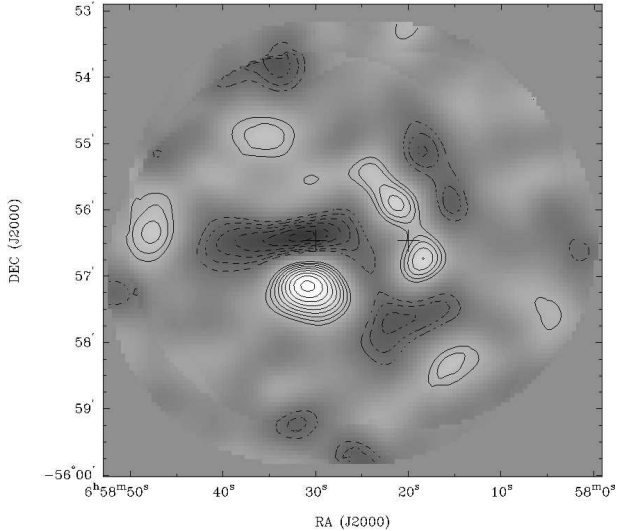


Figure 4. Source-subtracted non-deconvolved 18 GHz mosaic image of the bullet cluster, made with natural weighting and a uv taper corresponding to a $39'.8 \times 32'.1$ FWHM beam. Image rms noise level is $6.5 \mu\text{Jy beam}^{-1}$. Contour levels are at $\pm(3,4,5,6,7,8,9,10)$ times the rms noise. The radio halo previously detected by Liang et al. (2000) is the brightest positive feature close to the centre of the image and has a peak of 7.8σ ; the SZ effect is detected and has a peak decrement of -10.7σ to the S of the halo. Two other SZ effect features are detected to the NW regions of the halo, with a peak decrement of -5.7σ . Contrast has been adjusted in this image in order to make all contours visible. The two peaks seen in X-rays are marked. Notice the $\sim 40''$ displacement of the peak SZE decrement from the X-ray brightness peak

It is possible to compare the derived Compton- y parameter from our observations and compare it with the derived Compton- y from the APEX-SZ observations of Halverson et al. (2009) even though they do not derive a Compton- y from the peak SZE they observe. We estimate it from the peaks of the SZE in the two observations – those presented in this paper and those in Halverson et al. (2009) – and compare them. The Compton- y parameter from our data (without radio halo subtraction) is $y=7.0 \times 10^{-5}$ whereas the Compton- y from Halverson et al. (2009)'s observations is $y=2.95 \times 10^{-4}$. Our 18 GHz ATCA image of the SZE distribution is an interferometer image and would miss larger scale extended features. The smallest projected baselines in the ATCA observations correspond to the antenna diameter of 22 m, and the largest angular scale structures reproducible in the ATCA image would be less than the antenna beam FWHM of $2'.6$. Because of missing large-scale

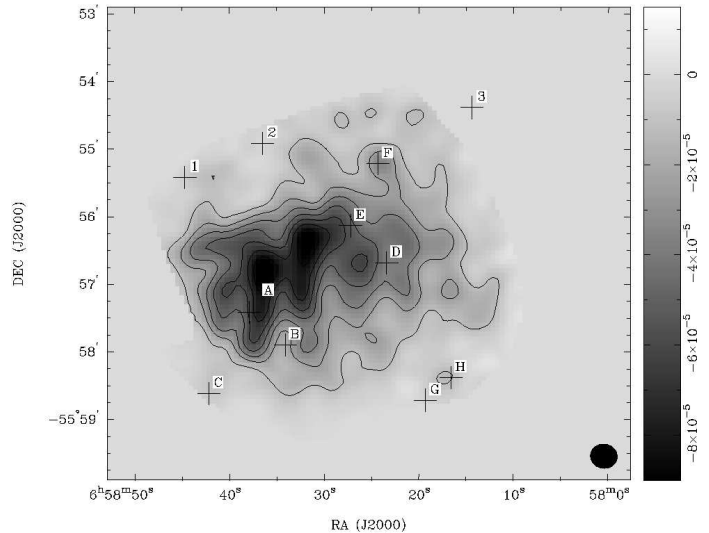


Figure 5. An image of the radio halo in the Bullet cluster. This image was obtained by convolving the 1.344 GHz radio halo image with the 18 GHz synthesized beam and then applying a gain taper for the primary beam at 18 GHz.

Table 3. Unresolved continuum radio sources detected in the Bullet cluster field.

Source	RA (J2000) DEC						Flux Density
	h	m	s	°	'	''	$S_{18 \text{ GHz}}$ (mJy)
A	06	58	38.0	-55	57	25	1.69 ± 0.04
B	06	58	33.8	-55	57	58	0.06 ± 0.04
C	06	58	41.4	-55	58	41	1.4 ± 0.4
D	06	58	23.8	-55	56	41	0.07 ± 0.02
E	06	58	27.5	-55	56	06	0.05 ± 0.02
F	06	58	24.5	-55	55	13	0.11 ± 0.03
G	06	58	19.3	-55	58	41	0.26 ± 0.12
H	06	58	16.1	-55	58	24	0.13 ± 0.08
1	06	58	44.6	-55	55	24	0.5 ± 0.2
2	06	58	36.7	-55	54	57	0.18 ± 0.06
3	06	58	14.6	-55	54	23	0.53 ± 0.13

NOTES– Letters indicate discrete sources listed in Liang et al. (2000) and have the same letters as in their Table 2; numbers indicate additional discrete sources from our 18-GHz observations.

SZE structure the absolute depth of SZE features might be reduced.

The discrepancy between the Compton- y computed in the ATCA image compared to the APEX image shows that the SZE is not just the compact features detected in this work, and halo subtraction and sensitivity to larger scale

SZE features are important to image the SZE in this cluster in its entirety.

In the next section, we describe consistency checks on our data and 18 GHz images, to prove that the SZ feature discussed above is not an artifact of improper deconvolution or incorrect point-source removal.

4 TESTS OF ROBUSTNESS / ERROR ESTIMATES

4.1 Error Estimates for point-source residuals

4.1.1 Point-source subtraction error estimate

Sidelobe level at the SZE peak dip and the Radio Halo peak sites due to each unresolved continuum source was estimated, from the beam pattern corresponding to the image in Fig. 8. These values are stated as fractions in Table 5, in columns 4 and 5. Next, the residuals at the point-source sites are estimated; these are listed in column 6 in Table 5 as fractions of the noise rms. Estimates of the errors caused due to sidelobes of these residuals were then estimated; these are listed in the last two columns in the same table. A worst case error in flux density at the position of the hole is estimated by summing these error contributions; the value of this error estimate is less than 0.06σ or $0.38\mu\text{Jy beam}^{-1}$, for both the SZE peak dip and the RH peak. The contribution to uncertainty from point-source subtraction is thus not significant.

4.2 Comparison of SZ feature before and after point-source subtraction

Fig.(1) shows the 18 GHz image with all point-sources present; this image has a -ve feature peaking at RA: $06^{\text{h}}58^{\text{m}}30^{\text{s}}.285$, DEC: $-55^{\circ}57'08''$ at -11.1σ ($-87.5\mu\text{Jy beam}^{-1}$; noise RMS = $6.5\mu\text{Jy beam}^{-1}$). After modeling and removing all point-sources, this -ve feature is still present, with its peak still at at RA: $06^{\text{h}}58^{\text{m}}30^{\text{s}}.285$, DEC: $-55^{\circ}57'08''$, and a peak of -10.7σ ($-84.7\mu\text{Jy beam}^{-1}$; noise RMS = $6.5\mu\text{Jy beam}^{-1}$, i.e. a difference of $2.8\mu\text{Jy beam}^{-1}$). More importantly, the size, extent and shape of this -ve feature remain exactly the same after point-source subtraction. We summarize the properties of the -ve (SZ) feature before and after point-source subtraction in Table 4. From the table, we may conclude the following errors/limits on the properties of the the SZE feature:

- (i) Error in Intensity: $\pm 2.8\mu\text{Jy beam}^{-1}$
- (ii) Error in Significance: $\pm 0.4\sigma$
- (iii) Error in Position: $\pm 0''$
- (iv) Error in Size: $< 1''$

4.3 Comparing 2009 and 2010 datasets

Our 18 GHz data was collected in two different arrays of the ATCA: H168 and H75, in 2009 and 2010. Both the 2009 and 2010 datasets contain data from both the arrays. We can therefore test the validity of the features in the 18 GHz image by comparing images from the 2009 and 2010 datasets.

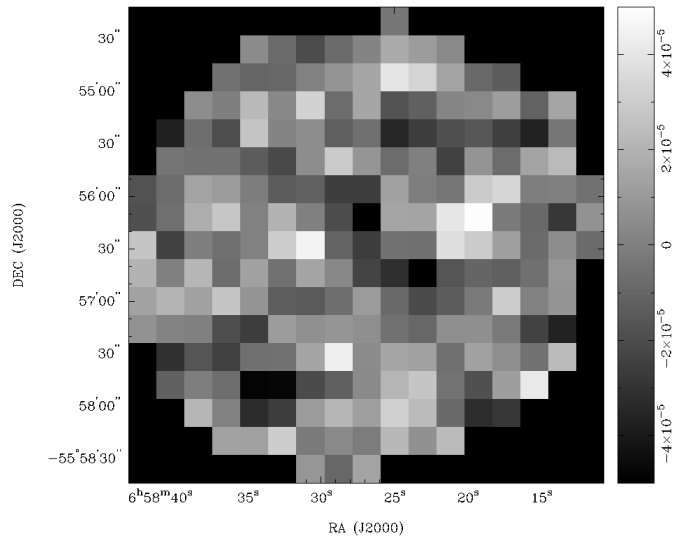


Figure 6. The difference between images made with the 2009 and 2010 datasets. Noise RMS is $20\mu\text{Jy beam}^{-1}$, and this difference image is consistent with gaussian noise.

A difference of the images made from the two datasets was taken – these images were made with a resolution of $16''$, to ensure that the pixels are independent data samples. The difference is shown in Fig.(6). This difference image was compared with a gaussian with RMS $20\mu\text{Jy beam}^{-1}$, using the non-parametric Mann-Whitney Wilcoxon test, and it was found that z-value=0.7 and 2-tailed p-value=0.43. The difference image is therefore consistent with gaussian noise.

This means that the features are not a result of phase errors in calibration.

4.4 Comparing the shape and size of the SZ effect at 18 GHz to the 90 GHz APEX image

The shape and size of the SZ effect in our 18 GHz may be compared to the 90 GHz APEX single-dish image, provided that a reliable model of the radio halo at 18 GHz exists. It is not possible to separate the radio halo and the SZ given observations at a single frequency, but a few reasonable assumptions may be made about the radio halo, in order to estimate the SZ at 18 GHz. These are described in §5.1 and §5.2. The resulting 18 GHz SZ images were convolved to a $90''$ beam, as shown in Figs.(9&11). These are qualitatively similar to Fig.(3) in (Halverson et al. 2009). This is discussed in further detail in §5.1.

5 LIMITS ON THE SZ EFFECT FROM 18 GHz ATCA IMAGE

In this section we enumerate and examine different possibilities for the properties of the radio halo and the SZE and provide upper and lower limits on the peak of the SZE from our observations, combined with those made by Liang et al. (2000). Our ATCA image misses the largest scales (i.e. lowest uv-spacings), and all discussion below pertains to the angular scales covered by our image.

Table 4. A comparison of the compact SZ feature properties before and after point–source subtraction.

Label	RMS _{NOISE}	Intensity	Significance	Size	RA (J2000) DEC					
	($\mu\text{Jy beam}^{-1}$)	($\mu\text{Jy beam}^{-1}$)	(σ)	(3σ contour)	h	m	s	°	'	"
Before	6.5	35.2	5.8	$64'' \times 56''$	06	58	30.285	−55	57	08
After	6.5	84.7	10.7	$64'' \times 56''$	06	58	30.285	−55	57	08

NOTES– The shape of the SZ feature remains unchanged; positional differences between 3σ contours of the SZ feature before and after point–source subtraction are $<1''$.

Table 5. Sidelobe levels at the SZE and Radio Halo feature peaks

Source	Distance (") from		Sidelobe levels at		Residual (σ)	Residual \times Sidelobe	
	RHM	SZM	RHM	SZM		RHM (σ)	SZM (σ)
A	56	53	0.0068	−0.0096	0.5	0.0340	−0.0480
B	103	56	−0.0086	−0.0370	−0.6	0.0052	0.0222
C	125	124	0.0100	−0.0140	−1.3	−0.0130	0.0182
D	146	79	0.0015	−0.0030	0.2	0.0003	−0.0006
E	119	70	−0.01600	−0.0145	−0.3	0.0048	0.0043
F	145	120	−0.0050	0.0035	−2.0	0.0200	−0.0140
G	160	147	0.0090	0.0135	−1.6	−0.0144	−0.0216
H	236	158	0.0068	0.0130	−3.0	−0.0204	−0.0390
1	77	143	−0.0063	0.0170	0.5	−0.0032	0.0085
2	106	131	0.0130	0.0020	−2.0	−0.0260	−0.0400
3	252	212	0.0080	−0.0065	−2.0	−0.0160	0.0130
Sum:			+0.0192	−0.0426		−0.0593	−0.0538

NOTES– In this table, as later, we denote the peak SZE dip position by ‘SZM’ and the peak of the radio halo by ‘RHM’.

We first made an image of the Radio Halo from Liang et al. (2000), extrapolated to 18 GHz, using the spectral index quoted by them. In order to ensure the same uv–coverage, we convolved the Liang et al. (2000) image with the synthesized beam at 18 GHz. We then weighed this image with a taper representing the primary beam of the ATCA at 18 GHz. This results in a radio halo image that has the same uv–coverage as our 18 GHz image, and is weighed with a taper representing the beam at 18 GHz. This image can now be used to put limits on the SZE at 18 GHz, as described below.

In what follows, we denote the peak SZE dip position by ‘SZM’ and the peak of the radio halo by ‘RHM’. We enumerate and discuss the possibilities for radio halo properties below, assuming that the radio halo has a spectral index of -1.3 between 1.344 and 6 GHz, as measured by Liang et al. (2000). Any spectral index variations mentioned in the following discussion are between 6 and 18 GHz.

5.1 Hypothesis I: The Radio Halo retains its properties up to 18 GHz

The radio halo image we obtained, as described above, was multiplied the result with a factor that represents a spectral index of -1.3 , the value quoted by Liang et al. (2000). We subtracted this from our 18 GHz image, and resulting image is shown in Fig.(7). We then convolved this image to $45''$, obtaining the image shown in Fig.(8). Brunetti et al. (2009) discuss spectral index variations at $\nu > 10$ GHz, and from their discussions of primary, secondary and hybrid models

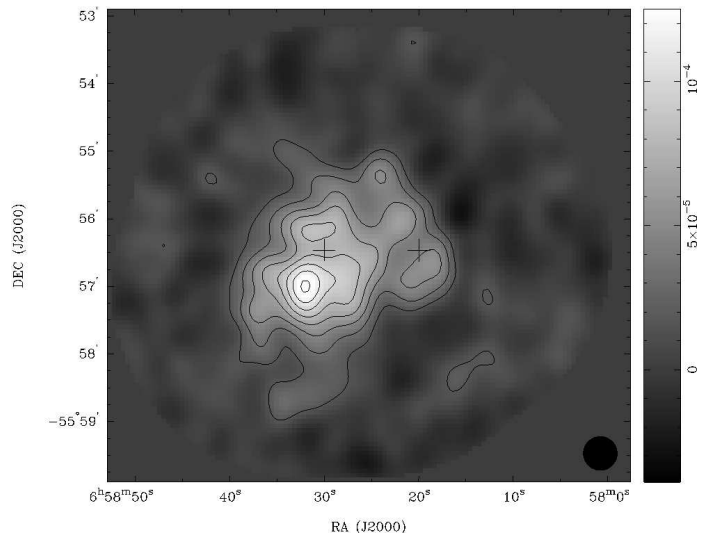


Figure 7. 18 GHz mosaic image of the SZE in the Bullet cluster, with the radio halo subtracted assuming $\alpha = -1.3$ between 1.344 and 18 GHz, as measured by (Liang et al. 2000); the image has been smoothed to a beam of FWHM $30''$. Contours are at $(-2, -4, -6, -8, -10, -12, -14, -16)$ times the image rms noise of $8.0 \mu\text{Jy beam}^{-1}$. Brightness centres of X–ray emission are marked.

of radio halo generation, it is unlikely that the radio halo in the Bullet cluster retains its spectral index and does not steepen at frequencies above 10 GHz. The image in Fig.(8)

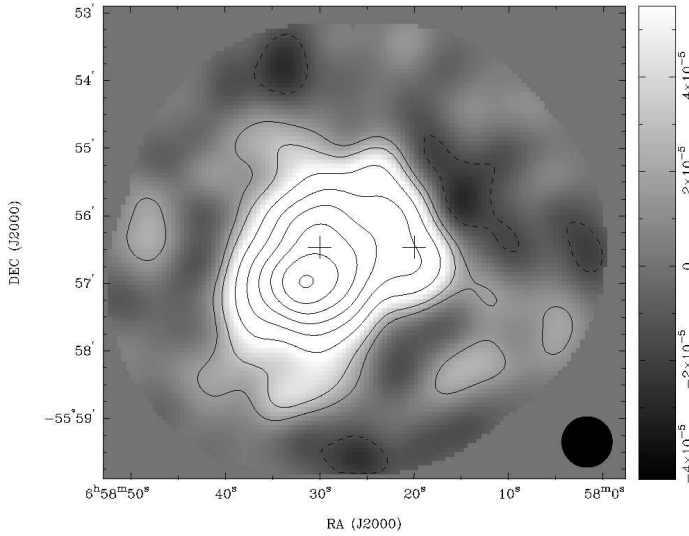


Figure 8. 18 GHz mosaic image of the SZE in the Bullet cluster, with the radio halo subtracted assuming $\alpha = -1.3$, as measured by (Liang et al. 2000); the image has been smoothed to a beam of FWHM $45''$. Contours are at $(-28, -24, -20, -16, -14, -12, -8, -4, -2, 2)$ times the image rms noise of $8.0 \mu\text{Jy beam}^{-1}$. Brightness centres of X-ray emission are marked, as in the previous image.

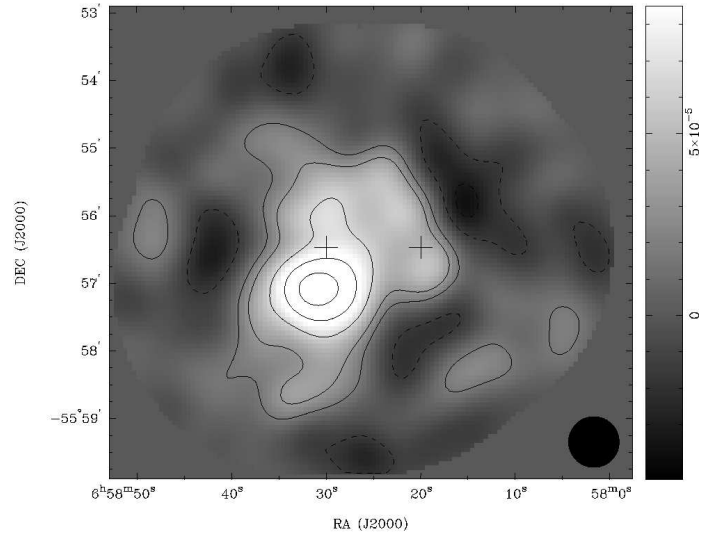


Figure 10. 18 GHz mosaic image of the SZE in the Bullet cluster, with the radio halo subtracted assuming $\alpha = -1.3$ between 1.344 and 6 GHz and $\alpha = -2.0$ between 6 and 18 GHz; the image has been smoothed to a beam of FWHM $45''$. Contours are at $(2, -2, -4, -8, -12, -15)$ times the image rms noise of $8.0 \mu\text{Jy beam}^{-1}$. Brightness centres of X-ray emission are marked, as in the previous image.

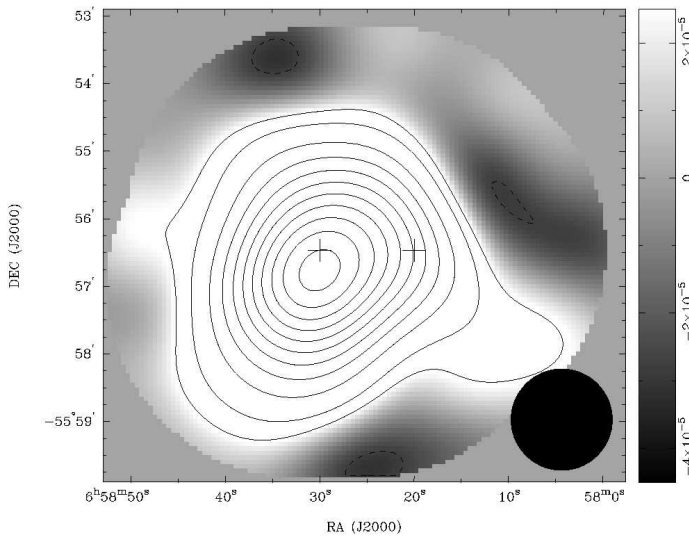


Figure 9. 18 GHz mosaic image of the SZE in the Bullet cluster, with the radio halo subtracted assuming $\alpha = -1.3$, as measured by (Liang et al. 2000); the image has been smoothed to a beam of FWHM $90''$. Contours are at $(2, -2, -4, -8, -12, -16, -20, -24, -28, -32, -36, -40)$ times the image rms noise of $14.0 \mu\text{Jy beam}^{-1}$. Brightness centres of X-ray emission are marked, as in the previous image.

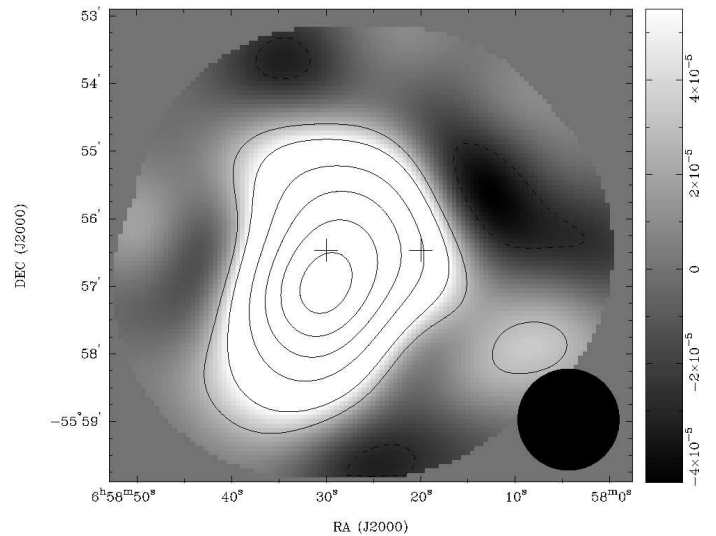


Figure 11. 18 GHz mosaic image of the SZE in the Bullet cluster, with the radio halo subtracted assuming $\alpha = -1.3$ between 1.344 and 6 GHz and $\alpha = -2.0$ between 6 and 18 GHz; the image has been smoothed to a beam of FWHM $90''$. Contours are at $(-2, -4, -8, -11, -15, -20)$ times the image rms noise of $14.0 \mu\text{Jy beam}^{-1}$. Brightness centres of X-ray emission are marked, as in the previous image.

is therefore an upper limit to the SZE in the Bullet cluster at 18 GHz, given the ATCA uv-coverage.

The peak SZE dip at SZM is $-227 \mu\text{Jy beam}^{-1}$, which corresponds to a Compton- y of 1.7×10^{-4} . Even after subtracting the maximum possible radio halo contribution and convolving with a $45''$ beam, the Compton- y at 18 GHz is less than that measured by the APEX single-dish instru-

ment [REF]. This clearly indicates missing large-scale structure. However, the shape of the SZ effect at 18 GHz is similar to that of the SZ image at 90 GHz obtained from APEX. On convolving the radio halo subtracted image to $90''$ (see Fig.(9)), the shape and size of the SZ image at 18 GHz qualitatively resembles the shape and size of the SZ image at 90 GHz. This indicates that the missing large-scale structure in

SZ is probably a smooth envelope that encompasses multiple compact features that are detected in the ATCA image and are spread over the SZE extent. In this scenario, our image detects substructure and this is distributed over the SZE extent suggesting that turbulence in gas pressure owing to the merger is widespread. However, it is well known that Fourier synthesis imaging of extended emission with high angular resolution tends to represent smooth structure as a patchy image arising from calibration errors and deconvolution instabilities. We present in Fig. 4 a non-deconvolved source-subtracted image of the Bullet cluster, which is similar to the deconvolved image in Fig. 3.

Additionally, we have compared two independent datasets in §... above and confirmed that the substructure is identical within the expected errors associated with image noise. We have also shown in above that the contribution from point-source residuals to the error in the peaks of the radio halo and SZE is insignificant; being a small fraction of the noise rms ($<0.06\sigma$).

5.2 2-phase spectral index

(Brunetti & Lazarian 2011) have shown that in turbulent (re-)acceleration models of radio halo formation, a steepening, or “knee” is expected in the spectrum of the radio halo. The frequency at which this “knee” occurs is indicative of the age of the non-thermal plasma, and the relative epoch of its (re-)acceleration, i.e. the epoch of the cluster merger. Several radio halos known to be associated with cluster mergers exhibit this steepening. The steepest known spectral index for a radio halo is $\alpha=2.0$. As mentioned earlier, the measurement of the spectral index of the radio halo in the Bullet cluster is robust to at least 6 GHz; therefore, we may build a simple model of the radio halo spectral index, in which $\alpha=1.3$ from 1.344 to 6 GHz and $\alpha=2.0$ from 6 to 18 GHz. This model was then subtracted from our 18 GHz image, and the subtraction followed the same steps described in the previous sub-section. The result of this subtraction, convolved with a $45''$ beam, is shown in Fig.(10). The peak SZE dip at SZM is $-145\mu\text{Jy beam}^{-1}$, which corresponds to a Compton- γ of 1.1×10^{-4} .

5.3 Spatial spectral index variations

Though Liang et al. (2000) rule out spatial variations in the radio halo spectral index between 1.344 and 9 GHz, halo formation models do not rule out spatial variations in the spectral index above 10 GHz. In general, a flat index at RHM and a steep spectrum at SZM would minimize the SZE. We therefore simulated such a spectral index which would de-emphasize the SZE, in order to explore the effect of extreme variations of the spectral index on the nature of the SZE, as follows.

First, the compact feature in Fig.(2) was modeled as a gaussian and its properties (RA, Dec, major axis, minor axis) noted. Then, a gaussian spectral index map (for the radio halo) was simulated centered at the position of the compact SZE feature in Fig.(2), so that the index would be steepest at the centre of the gaussian derived above, and would flatten out in the outer regions of the gaussian. The value chosen at the centre was such that only $\sim 10\%$ of the

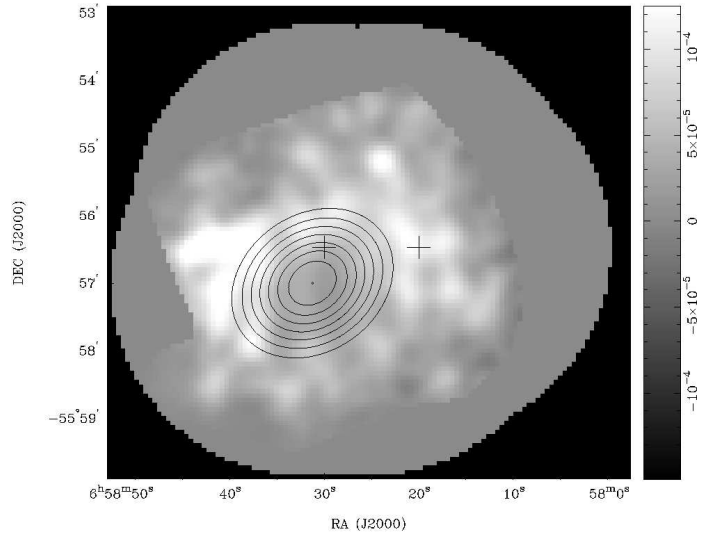


Figure 12. A model of the radio halo at 18 GHz, given the spectral index model which de-emphasizes the compact SZE feature, shown as a contour.

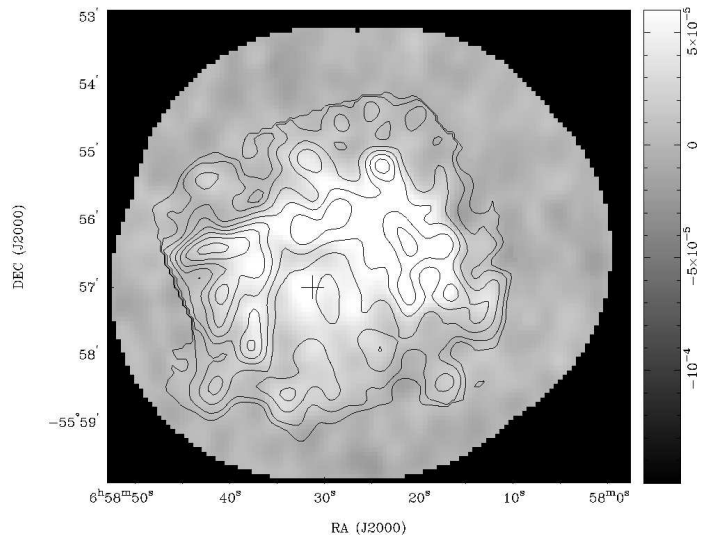


Figure 13. The result of subtracting the extreme halo in Fig.(12) above, with contours of the radio halo model at 18 GHz (shown in the previous figure). The subtraction clearly leads to several compact features, most of which are caused by the compact features in the radio halo model. However, the compact SZ feature seen in our original 18 GHz feature is still present. As discussed in the text, this implies that a simple spatial variation that de-emphasizes the radio halo at the SZM is not sufficient to make the compact SZE feature go away.

radio halo would be present at the centre of the compact SZE feature at 18 GHz. This spectral index map is shown as a contour in Fig.(12). The radio halo image, weighed by the appropriate taper, as described above, was then multiplied with a factor that represents a constant spectral index between 1.344 and 6 GHz, and a spectral index variation we simulated above, for frequencies between 6 and 18 GHz. The resulting image of the radio halo at 18 GHz is shown in Fig.(12). This image represents the radio halo at 18 GHz,

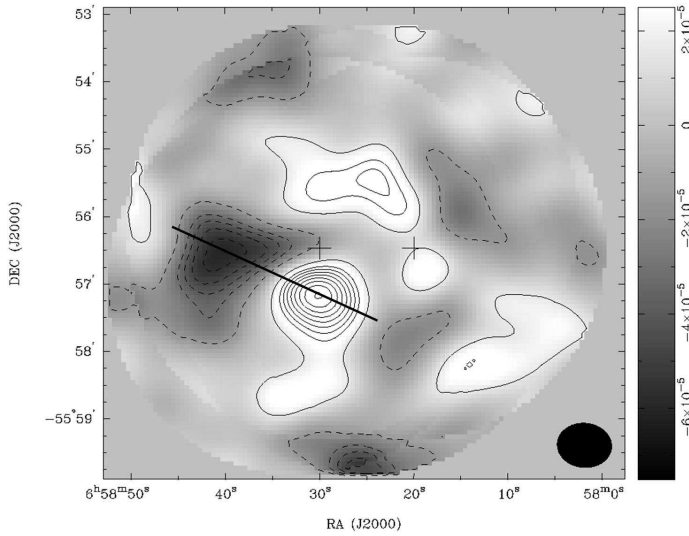


Figure 14. A slice connecting SZM and RHM, and including the entire extent of the SZE feature as well as the radio halo.

given the simulated spectral index, and was subtracted from our 18 GHz image, resulting in the image shown in Fig.(13).

The resulting SZE image in Fig.(13) clearly has many compact SZE features. This implies that the compact SZE feature seen in Fig.(2) is not merely an artifact of simple (smooth) spatial spectral index variations. The figure clearly suggests that a different approach is needed in order to de-emphasize the compact SZE feature – the radio halo must have a different variation in order for the compact feature to be absent. We explore the simplest such variation below.

5.4 Constraints on Radio Halo properties needed to rule out a compact feature

Since a simple de-emphasizing of the SZE in the previous section did not yield an SZE image with no compact features, we now attempt to find the radio halo distribution at 18 GHz, which, when subtracted from our 18 GHz image, would yield a uniform SZE over the entire region of the cluster. We do this analysis first along a line connecting the SZM and the RHM, and then for the entire image, as described below.

5.4.1 One-dimensional analysis

A slice connecting the SZM and the RHM was taken, as shown in Fig.(14). A plot of intensity values along the slice is shown in Fig.(15). If the SZE was a large, diffuse feature, it would be a constant over this slice. The *least* value of this constant would be the same as the lowest value in the plot in Fig.(15), i.e. $-90\mu\text{Jy beam}^{-1}$. We therefore assume that the diffuse SZE will have this value – this will yield the *minimum* spatial variations in the spectral index needed to have a non-compact SZE.

First, the above value ($-90\mu\text{Jy beam}^{-1}$) was subtracted from the intensity vs. position plot, yielding the *minimum amount* of radio halo emission at 18 GHz, as shown in Fig.(18). Next, the same slice was taken in the 1.344 GHz radio halo image, as shown in Fig.(16). The spectral index

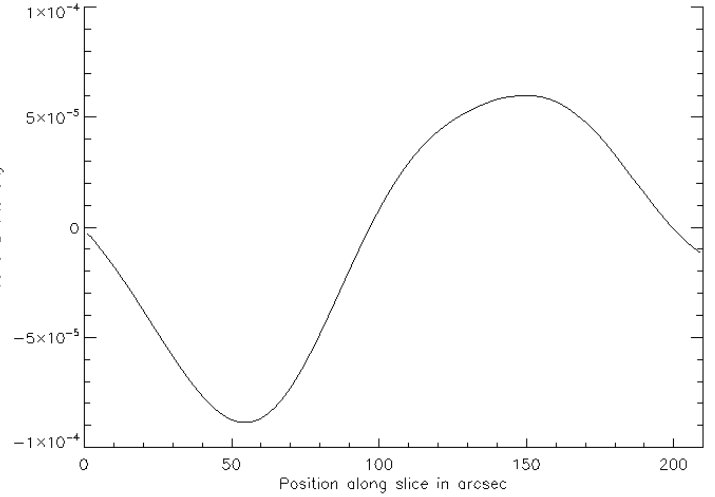


Figure 15. A plot of intensity along the slice shown in Fig. 14. This plot starts from the bottom right corner of the slice in Fig. 14.

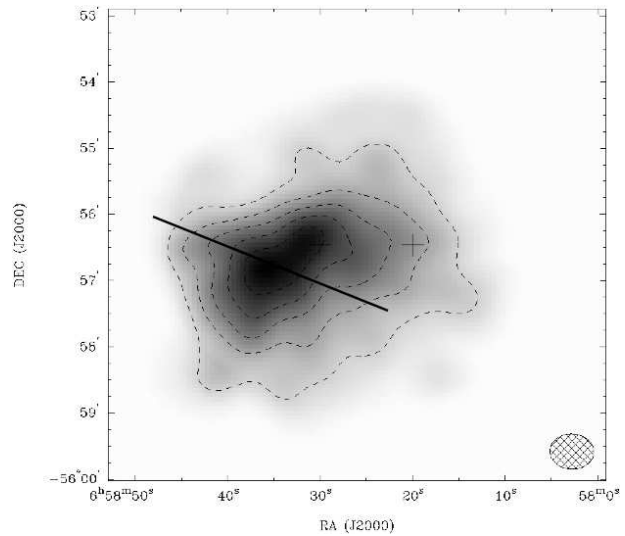


Figure 16. The same slice as in the previous figure, on the radio halo image.

may now be calculated as a function of the minimal 18 GHz radio halo intensity along the slice, as shown in Fig.(19) (I_{18}), 6 GHz intensity (I_6 ; since the spectral index is known to be constant between 1.344 and 6 GHz, from Liang et al) and therefore, distance, from the following relations

$$I_6 = I_L \left(\frac{6}{1.344} \right)^{-1.3} \quad (1)$$

$$I_{18} = I_6 \left(\frac{18}{6} \right)^{-\alpha} = I_L \left(\frac{6}{1.344} \right)^{-1.3} \left(\frac{18}{6} \right)^{-\alpha} \quad (2)$$

And so,

$$\alpha = \frac{\log(I_{18}) - \log(I_L) + 1.3 \log\left(\frac{6}{1.344}\right)}{\log\left(\frac{1}{3}\right)} \quad (3)$$

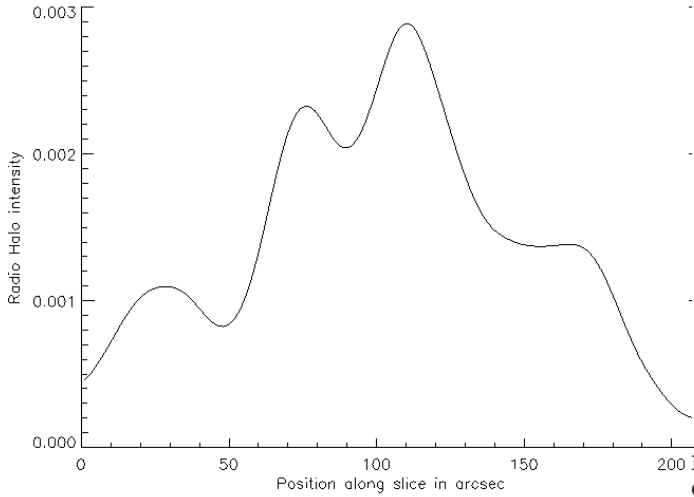


Figure 17. A plot of intensity along the slice shown in Fig. 16. This plot starts from the bottom right corner of the slice in Fig. 16.

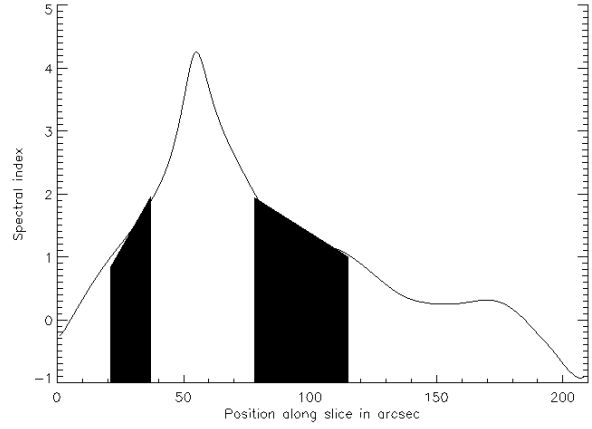


Figure 19. Variation of the spectral index (between 6 and 18 GHz) as a function of distance along slice which is needed to make the SZ feature in the 18 GHz image non-compact. This spectral index is derived from the minimum radio halo level needed to make the SZ feature non-compact, shown in Fig. 18. The area that has $2 > \alpha > 1$ is marked in the figure. Notice that only $\sim 25\%$ of the plot has a spectral index $2 > \alpha > 1$. The region around SZM needs to have a very steep spectrum in order for the SZE feature to be non-compact. This kind of extreme variation in the spectral index ($4 > \alpha > 0.1$) has never been observed in any radio halo, because radio halos are produced by synchrotron.

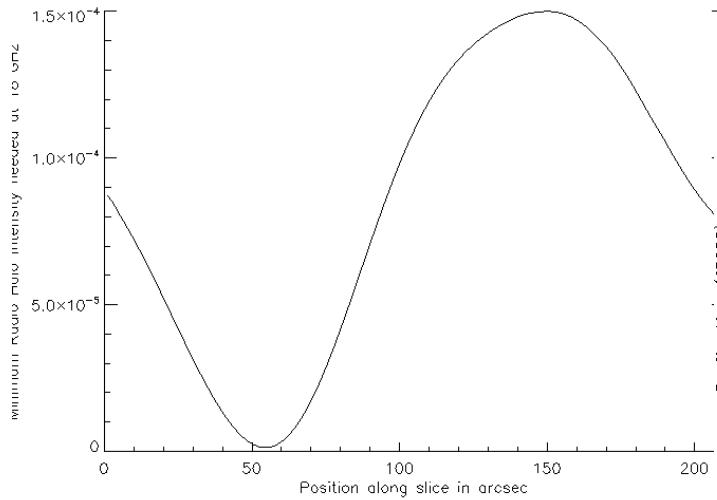


Figure 18. A plot of the minimum Radio Halo intensity needed to make the SZ in the 18 GHz image non-compact. This is obtained by subtracting the peak dip of the SZ feature from the radio halo intensity along the slice defined in the above figures.

α is plotted in Fig.(19). Most ($\sim 75\%$) of the points in the spectral index plot lie outside the known and observed range $2 > \alpha > 1$. For a small subset of points in the plot, the spectral index is inverted - this extreme/peculiar behaviour of the spectral index is not possible to explain physically, through any existing model or process. This extreme variation in the spectral index is therefore not likely to occur, and indeed, is presented here to emphasize the compact nature of the SZE in the Bullet cluster.

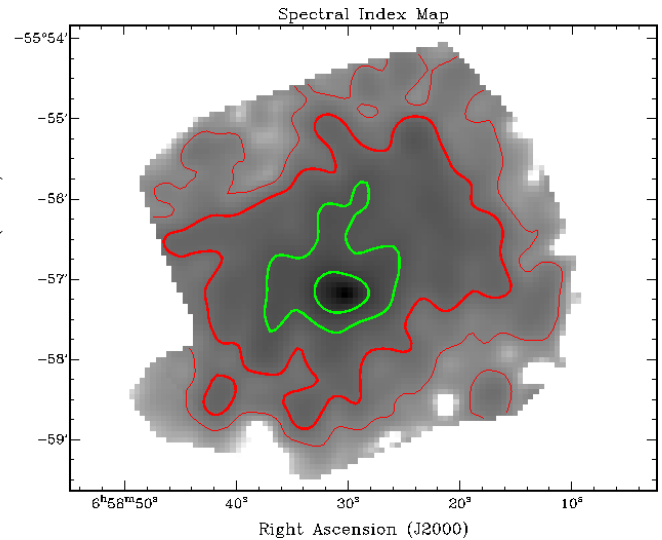


Figure 20. An image of the spatial variation of the spectral index (between 6 and 18 GHz) as a function of position. The area that has $2 > \alpha > 1$ is marked between the two green contours in the figure. Notice that only $\sim 25\%$ of the plot has a spectral index $2 > \alpha > 1$. The region around SZM needs to have a very steep spectrum in order for the SZE feature to be non-compact. This kind of extreme variation in the spectral index ($4 > \alpha > 0.1$) has never been observed in any radio halo, because radio halos are produced by synchrotron.

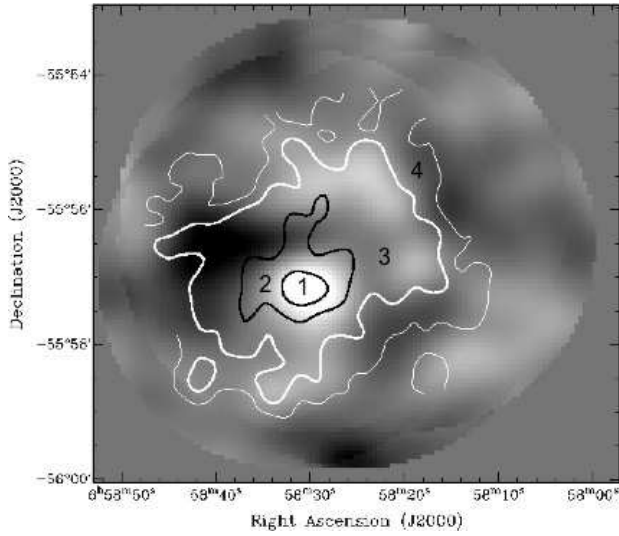


Figure 21. Our 18 GHz image, with an overlay of contours of the spectral index needed between 6 and 18 GHz in order to make the SZ feature non-compact. Regions with different ranges are marked in the figure as follows. Region 1: $4 \leq \alpha < 2$; Region 2: $2 > \alpha > 1$; Region 3: $1 > \alpha > 0$; Region 4: $\alpha > 0$. Notice that region 2 has $< 25\%$ of the area in the index contour.

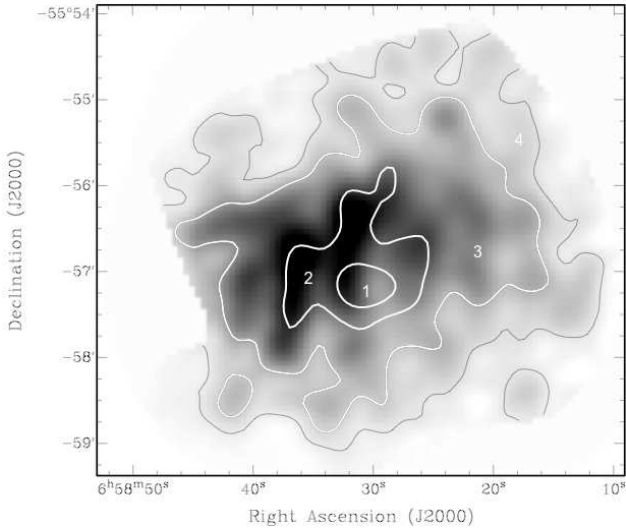


Figure 22. 1.344 GHz image from (Liang et al. 2000), with an overlay of contours of the spectral index needed between 6 and 18 GHz in order to make the SZ feature non-compact. Regions with different ranges are marked in the figure as follows. Region 1: $4 \leq \alpha < 2$; Region 2: $2 > \alpha > 1$; Region 3: $1 > \alpha > 0$; Region 4: $\alpha > 0$. Notice that region 2 has $< 25\%$ of the area in the index contour.

5.4.2 Image analysis

The process described in the previous section can be applied to the entire 2-dimensional image instead of a single slice. Eq.(3) then denotes the spectral index α as a function of (RA,Dec.). We applied eq.(3) to Fig.(2), our 18 GHz image, and an extrapolation of Fig.(5) to 6 GHz using the spectral index measured by (Liang et al. 2000), in order to obtain the

spectral index map required for the SZ feature to be non-compact. This spectral index map is shown in Fig.(21&22).

It is more useful to overplot the contours of this spatial variation of the spectral index on our 18 GHz image as well as the radio halo; these overplots are shown in Figs.(21&22) respectively. From Fig.(21), it is clear that the region with the deepest SZE coincides with the region that has the steepest spectral index, $4.0 > \alpha > 2.0$. This range for the spectral index is far beyond the limits obtained from observations of radio halos thus far. The reason that spectral indices this steep have never been observed (and are not likely to be observed) is that radio halos are caused by synchrotron emission. A steepening in radio halo emission from the region with a deep SZE implies a steepening in the Energy spectrum of electrons in that region. This is unlikely, given that $SZE \propto \int n_e T_e dl$. Therefore, a spectral index steepening in a deep SZE region is physically inconsistent.

Additionally, spectral indices of $\alpha < 1$ have not been observed, whereas we find large regions with this spectral index in Fig.(21). A relatively flat spectral index of $1 > \alpha > 0.7$ may be expected in the hottest and most turbulent regions in the ICM of clusters that have undergone recent mergers. However, flattening is not likely to occur a significant distance away from the most turbulent and hottest regions of the ICM, which is what we observe in the spectral index map in Fig.(20).

We may therefore conclude that in trying to rule out a compact SZE feature, we have admitted physically inconsistent ranges of spectral indices in a large ($> 75\%$) region of the ICM in the Bullet cluster. This attempt to rule out a compact SZE feature is also, therefore, a failure.

In order to obtain further constraints on the SZE and the radio halo, the two components need to be separated through multi-frequency observations; a comparison of 18 GHz and 150 GHz images can lead to SZE-halo separation; however, uv-coverages of the ATCA and APEX instruments is complementary (since APEX is a single-dish experiment). Single-dish measurements of the Bullet cluster at 18 GHz are therefore needed to separate radio halo and SZE.

6 A DISCUSSION OF THE SZE IN THE BULLET CLUSTER

The sky distribution in the SZE does indeed coincide with the radio halo distribution in the western and southern parts; additionally, in our high-angular resolution interferometer image, SZE is also detected towards the western end of the radio halo in two distinct features in the NW and SW parts of the image. The significance of the peak dips in these features is 4.0σ and 5.5σ (times the noise RMS of $8.0\mu\text{Jy beam}^{-1}$) respectively, in Fig.(2) – without radio halo subtraction.

We emphasize that the SZE appears as a compact feature. The deepest SZE feature is at RA: $06^{\text{h}}58^{\text{m}}30^{\text{s}}.285$, DEC: $-55^{\circ}57'12''$ in Fig.(2) and is clearly offset $65''$ to the SE of the eastern X-ray emission peak; this deep SZE hole is a flux density decrement of $-88.8\mu\text{Jy/beam}$

Significantly differing depths in the SZE decrement in the APEX and ATCA images imply that there is substantial extended SZE structure in the Bullet cluster on angular

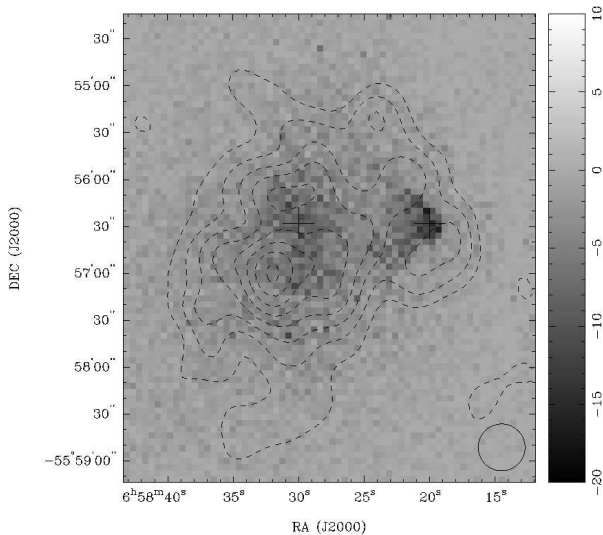


Figure 23. X-ray greyscale overlaid with contours of SZE obtained after subtracting the radio halo assuming a spectral index of $\alpha = 1.3$ from 1.344 to 18 GHz. Contour levels are at $(-2, -4, -6, -8, -10, -12, -14, -16)$ times the noise RMS of $6.5 \mu\text{Jy beam}^{-1}$.

scales of $2/6$ and larger, which is resolved out and missing in the ATCA interferometer image.

Clearly, the data suggest the existence of a range of scales in the SZE structure in this merging cluster, requiring imaging with sensitivity to a range of spatial scales to produce a holistic image of the SZE. In Fig. 23 we show contours of the SZE overlaid on Chandra X-ray intensity distribution shown using grey scales.

We discuss in detail below the SZE features in our 18 GHz image:

(i) We observe a deep SZE ‘hole’ significantly displaced to the SE of the X-ray peak in the hotter eastern cluster. Since SZE probes integrated pressure along the line of sight, this suggests that there are significant pressure variations in the intracluster gas, presumably because of the ongoing cluster collision. X-ray spectral luminosity is proportional to $\int n_e^2 T^{-\frac{1}{2}} dl$, whereas the SZE is proportional to $\int n_e T dl$: the two effects represent different weightings of temperature T and electron density n_e . X-ray emission images are more representative of n_e distribution, whereas the SZE images are representative of T distribution. The offset of the SZE ‘hole’ from the emission peak suggests that the peak in intracluster gas temperature is spatially offset from the peak in gas density in the Bullet cluster². RXJ1347–1145 (Massardi et al. 2001; Mason et al. 2010) and CL0152–1357 (Massardi et al. 2010) are the only other clusters that display this offset, which is a demonstration of the complexity in intracluster gas distribution properties in merging clusters. We also observe significant SZE substructure across the cluster complex. All these SZE components are displaced from the peaks in X-ray emission corresponding to the two clusters comprising the Bullet cluster complex.

² Markevitch et al. (2002) have indeed reported finding highest temperatures SE of the X-ray peak.

(ii) All substructure we detect in the SZE image lies within the boundary of the radio halo. Moreover, careful examination of Fig.(7) indicates that the SZE in the western parts of the cluster complex appear to follow the contours of the radio halo. This has also been seen by Colafrancesco et al. (2011). This is surprising, since the radio halo arises from synchrotron plasma and the SZE from thermal intracluster gas and there is no spatial correspondence expected between these distinct components. A plausible reason for the cospatial locations of the SZE and radio halo—in the western parts of the cluster—is a common origin for the two populations of radiative electrons. Radio halos are believed to be synchrotron emission from electrons accelerated (or re-accelerated) to relativistic energies in the turbulence generated by cluster mergers. It may be that the radio halo was created in the turbulent wake of the passage of the ‘Bullet’ through the cluster gas, and the SZE also arises cospatially from relatively hotter electrons in the same turbulent wake. Absence of SZE towards the eastern parts of the radio halo would, in this picture, indicate longer lifetimes for the relativistic electrons compared to the SZE electrons. (Markevitch et al. 2002) have reported finding spatial correlation between halo brightness and local gas temperature in merging clusters; this is supplementary to the SZE and the halo being cospatial in our observations.

(iii) SZE dip is relatively shallow towards the peaks in the X-ray emission. In Fig. 23 it may be noted that the SZE contours are indented in sky regions where the X-ray emission is most intense. The observed avoidance of the highest emission measure regions by SZE suggests that the highest density parts of the cluster gas may have somewhat cooler temperatures, owing to shorter cooling timescales, and consequently contribute relatively less to the SZE.

(iv) The NW and SW SZE features are close to the shock fronts in the X-ray image, as is clear from Fig. 8. However, the SZE feature dips appear in front of the shock fronts, not behind – but shock fronts are the sites with highest pressure, and pressure peaks cannot appear in front of shocks. We may infer from this that the pressure peaks are behind or at the shock fronts, but due to no radio halo subtraction, the SZE dips appear to be in front of the shocks.

Massardi et al. (2010) have recently found a similar displacement of SZE dip from X-ray brightness peaks in the merging cluster CL0152–1357. In addition, this effect has been known to exist in the merging cluster RXJ1347–1145 (Komatsu et al. 2001; Mason et al. 2010).

7 SUMMARY

We have presented 18 GHz observations of the Bullet cluster from the ATCA, and report detection of substructure in the Sunyaev–Zeldovich Effect. We run through several tests of consistency to prove that the image of the SZE in the Bullet cluster is robust. We subtract unresolved continuum sources in the cluster field using 18 GHz ATCA images made with enhanced weightings to the longer visibility spacings. We run through two ways of ruling out a compact feature in the SZE, and arrive at the conclusion that inconsistent and non-physical steepening and flattening of the radio halo spectral index must be resorted to in order to rule out a compact SZE feature. We show that the most prominent SZ effect

feature in the 18 GHz image must be a compact feature, given reasonable assumptions about the Radio Halo. This deep SZE feature is significantly displaced from the peak in X-ray emission. The main conclusions from this work are:

- (i) High-frequency ($\nu > 10$ GHz) observations are crucial for probing the dynamics of energetic cluster mergers.
- (ii) The intracluster gas in the merging Bullet cluster appears to have significant pressure distribution structure that differs from that in gas emission measure, galaxy and dark matter distributions.

Future ALMA observations with a range of spatial frequencies would be expected to provide SZE images that reproduce the compact and extended structure together and hence be amenable to modeling of the gas in such merging clusters, where the pressure and temperature may have complex distribution structures. However, it may be noted that the synthesized of even the most compact sub-array in ALMA is too small, even at the lowest frequencies at which ALMA operates, to characterize the structures in the Bullet cluster (e.g. ALMA field-of-view at 100 GHz, the lowest operating frequency, is only $60''$; the smallest baselines of ~ 18 m yield an angular scale of $35''$). The total-power mode of ALMA is the only way that the large-scale structure of the SZE in the Bullet cluster can be characterized.

In order to enable a proper difference between the large-scale SZE at 150 GHz from APEX and the SZE at 18 GHz, leading to a characterization of the radio halo, a single-dish observation of the Bullet cluster at 18 GHz is needed. This measurement is possible using the 64 m Parkes Telescope in Australia.

ACKNOWLEDGMENTS

The Australia Telescope Compact Array is part of the Australia Telescope which is funded by the Commonwealth of Australia for operation as a National Facility managed by CSIRO.

Greyscale in Figure 23 courtesy of the Chandra X-ray Observatory Center, which is operated by the Smithsonian Astrophysical Observatory on behalf of NASA.

Travel to Australia was made possible by two travel grants from the Raman Research Institute, Bangalore, India and one from IUCAA, Pune, India.

We gratefully acknowledge a part of the observations being carried out by Dr. R. Subrahmanyan and Dr. M. Wieringa. We also thank Dr. D. Narasimha for motivating the search for SZ polarization.

SSM gratefully acknowledges the support provided by CSIR (Council for Scientific and Industrial Research), Government of India, through their grant number 03(1462)19-EMR-II.

REFERENCES

- Wilson, W.E. ... (33 authors including Malu, S.S.), 2011, MNRAS, Vol. 416, No. 2, pp. 832–856
 Lueker, M. et al., 2010, ApJ, 719, 2
 Sunyaev, R. A., Zeldovich, Ya. B., 1972, Comm. Astrophys. & Sp. Phys., 4, 173

- Andreani, P. et al., 1999, ApJ, 513, 23
 Clowe, D. et al., 2006, ApJL, 648, L109
 Halverson, N. W. et al., 2009, ApJ, 701, 42
 Liang, H. et al., 2000, ApJ, 544, 686
 Markevitch, M. et al., 2002, ApJL, 567, L27
 Rex, M. et al., 2009, ApJ, 703, 348
 Komatsu, E. et al., 2001, PASJ, 53, 1
 Mason, B. S. et al., 2010, ApJ, 716, 1
 Sault, R. J., 2003, ATNF Memo AT/39.3/124
 Massardi, M. et al., 2010, ApJL, 718, 1
 Plagge, T. et al., 2010, ApJ, 716, 2
 Birkinshaw, M., 1999, Phys. Rep., 310, 97
 Basu, K. et al., 2010, A&A, 519, A29
 Colafrancesco, S. et al., 2011, A&A, v.527, id.L1
 Brunetti, G., & Lazarian, A. 2011, MNRAS, 412, 817
 Cassano, R. 2010, A&A, 517, A10
 Cassano, R., Ettori, S., Giacintucci, S., et al. 2010, ApJL, 721, L82